ADVANCED FUNCTIONAL MATERIALS
www.afm-journal.de

Metavalent Bonding in Cubic SnSe Alloys Improves Thermoelectric Properties over a Broad Temperature Range

Nan Lin, Shuai Han, Tanmoy Ghosh, Carl-Friedrich Schön, Dasol Kim, Jonathan Frank, Felix Hoff, Thomas Schmidt, Pingjun Ying, Yuke Zhu, Maria Häser, Minghao Shen, Ming Liu, Jiehe Sui, Oana Cojocaru-Mirédin, Chongjian Zhou, Ran He,* Matthias Wuttig,* and Yuan Yu**

Monocrystalline SnSe is one of the most promising thermoelectric materials with outstanding performance and a high abundance of constituting elements. However, polycrystalline SnSe, which is more robust for applications, only shows large figure-of-merit (zT) values in its high-symmetry phase. Stabilizing the high-symmetry phase at low temperatures can thus enhance the average zT value over a broad temperature range. In this work, the high-symmetry rock-salt SnSe phase is successfully obtained by alloying SnSe with $AgVVI_2$ compounds (V = Sb, Bi; VI = Se, Te). These cubic SnSe phases show a unique portfolio of properties including a high optical dielectric constant, a large maximum of optical absorption, a large Born effective charge, and abnormal bond-breaking behavior in laser-assisted atom probe tomography. All of these characteristics are indicative of metavalent bonding. In contrast, the *Pnma* phase of SnSe employs covalent bonding. The enhanced symmetry at low temperatures is realized by tailoring chemical bonding. Concomitantly, zT near room temperature is increased by a factor of more than 10 from the pristine *Pnma* SnSe to *Fm*$\bar{3}$*m* SnSe alloys. This provides insights into the enhancement of the thermoelectric performance of SnSe and other chalcogenides over a broad temperature range by manipulating the chemical bonds.

1. Introduction

Tin selenide (SnSe) as a thermoelectric material has attracted considerable scrutiny since an extraordinarily high figure-of-merit (zT) of 2.6 at 923 K was reported in 2014 by Zhao et al.[1] Even though this high zT value has been questioned, in particular, questioning if it is an intrinsic property of single-crystal SnSe due to its ≈10% lower mass density compared to the theoretical value,[2,3] this does not refute that SnSe is a very promising thermoelectric compound.[4] For example, the zT values of SnSe single crystals can be substantially improved by judicious chemical doping such as Na,[5] Br,[6] Pb,[7] Cl,[8] and Cu.[9] However, the layered structure of SnSe single crystals causes serious mechanical instabilities, including weak strength and easy cleavage, strongly deteriorating its application potential.[10] On the contrary, polycrystalline SnSe compounds are considered more practical and deployable due to their

N. Lin, T. Ghosh, C.-F. Schön, D. Kim, J. Frank, F. Hoff, T. Schmidt, M. Häser, M. Shen, M. Liu, M. Wuttig, Y. Yu
Institute of Physics (IA)
RWTH Aachen University
Sommerfeldstraße 14, 52074 Aachen, Germany
E-mail: wuttig@physik.rwth-aachen; yu@physik.rwth-aachen.de

S. Han, C. Zhou
State Key Laboratory of Solidification Processing and Key Laboratory of Radiation Detection Materials and Devices
Northwestern Polytechnical University
Xi'an 710072, China
E-mail: cjzhou@nwpu.edu.cn

T. Ghosh
Department of Sciences and Humanities
Rajiv Gandhi Institute of Petroleum Technology
Jais, Amethi, UP 229304, India

P. Ying, R. He
Leibniz Institute for Solid State and Materials Research
IFW-Dresden
01069 Dresden, Germany
E-mail: r.he@ifw-dresden.de

The ORCID identification number(s) for the author(s) of this article can be found under https://doi.org/10.1002/adfm.202315652

DOI: 10.1002/adfm.202315652

low cost, ease of processing, and better mechanical properties.[4,11] Yet, the higher lattice thermal conductivity measured in polycrystalline SnSe not only limits its thermoelectric performance but also challenges the intrinsic low lattice thermal conductivity of monocrystalline SnSe.[12–16] In other words, the polycrystalline samples should show at least not higher lattice thermal conductivity than single crystals due to the presence of additional phonon scattering mechanisms at grain boundaries.[2] It has been first proposed by Zhao et al.[17] and then proved by Lee et al.[18] and Zhou et al.[19] that the presence of tin oxides at the grain boundaries of polycrystalline SnSe significantly increases the lattice thermal conductivity. Later, maximum zT values above 2.0 have been achieved in polycrystalline SnSe by removing oxides[19] or by chemical synthesis in conjunction with defect engineering.[20] Despite these big achievements, these polycrystalline samples only show high zT values at temperatures above 600 K.[13,15,16,20–22] This strongly reduces the overall energy conversion efficiency of polycrystalline SnSe. Especially for thermoelectric cooling, which has been demonstrated feasible and promising in monocrystalline SnSe,[9,23] the application of polycrystalline SnSe as coolers requires the improvement of near room-temperature zT values.

The excellent thermoelectric properties of SnSe at high temperatures are accompanied by a phase transition from a low-symmetry *Pnma* phase to a high-symmetry *Cmcm* phase with increasing temperature.[1,19–21] Indeed, high-symmetry chalcogenides such as PbTe[24] and GeTe[25] show excellent thermoelectric performance comparable to that in *Cmcm* SnSe. This naturally poses important questions: could we improve the thermoelectric properties of SnSe by stabilizing the high-symmetry phase at low temperatures and how do we realize the structural phase transition? It has been demonstrated that different crystal structures in chalcogenides[26,27] and even metals[28] are determined by differences in chemical bonding mechanisms. Manipulating structural transitions by tailoring chemical bonds has been successfully exemplified in GeSe alloys.[29–32] The *Pnma* GeSe phase transforms into the *R3m* phase and then the *Fm*$\bar{3}$*m* phase at room temperature by alloying with a series of compounds such as $AgSbTe_2$ and $AgSbSe_2$.[33,34] The latter two high-symmetry phases show an increase in zT by a factor of more than 10 compared to the *Pnma* phase. The *Pnma* GeSe phase employs covalent bonding. In contrast, the *R3m* and *Fm*$\bar{3}$*m* GeSe phases utilize metavalent bonding.[30,32] Given that SnSe and GeSe are isoelectronic compounds and share very similar electronic properties, it appears to be feasible to manipulate the crystal structure of SnSe by tailoring its chemical bonding as well. Indeed, cubic SnSe-based alloys have been realized in SnSe–$AgSbTe_2$,[35] SnSe–$AgSbSe_2$,[36] and SnSe–$AgBiSe_2$ alloys.[37] The increased entropy might offer a plausible explanation for the structural transition.[36,38] However, there are still no clear design rules about the selection of alloying compounds to increase the configuration entropy. Interestingly, only $AgVVI_2$-based compounds have shown efficacy in driving the structural transition of SnSe.[35–37,39] This phenomenon cannot be solely attributed to the increased entropy since numerous other ternary compounds should have yielded similar effects through entropy enhancement alone. In this regard, the impact of chemical bonding on this phase transition should also be explored.

In this work, the atomic arrangements of SnSe at ambient temperature and pressure are controlled by alloying with $AgVVI_2$ (V = Sb, Bi; VI = Se, Te). Structural characterizations, optical property measurements, bond-breaking investigations, and density functional theory (DFT) calculations are performed to identify the phase transitions and understand their origin. Subsequently, the thermoelectric properties of these alloys with different atomic arrangements are compared. We demonstrate that higher thermoelectric performance at low temperatures in polycrystalline SnSe can be achieved in a high-symmetry phase. This phase transition can be controlled by tailoring the underlying chemical bonding mechanism.

2. Results and Discussion

2.1. Structural Phase Transitions and Optical Properties

Polycrystalline SnSe–$AgVVI_2$ (V = Sb, Bi; VI = Se, Te) alloys were synthesized via melting raw elements in sealed quartz tubes at a high vacuum ($\approx 10^{-5}$ mbar) followed by spark plasma sintering (see the Experimental Section for details). The room-temperature powder X-ray diffraction (P-XRD) patterns shown in **Figure 1a** reveal that pristine SnSe at ambient conditions exhibits an orthorhombic crystal structure (*Pnma*), whereas the alloyed samples are dominated by cubic (*Fm*$\bar{3}$*m*) phase. This phase transition is further confirmed by Raman measurements as shown in Figure 1b. The pristine orthorhombic SnSe phase shows several Raman-active modes within the range of 23.5 to 160 cm^{-1}, consistent with the literature.[40] In contrast, the alloyed samples show no Raman active modes. This can be explained by the Raman selection rules, derived from group theory, which determine that the NaCl structure has no Raman active lattice vibrations. Additionally, all samples were measured via ultrafast reflection-type pump-probe spectroscopy. This technique allows for precise quantification of coherent phonon modes through femtosecond real-time reflectivity measurements.[41,42] In Figure 1c, the transient anisotropic reflectivity, measured through electro–optical sampling[29] (EO) of the various alloys, is depicted. Notably, only the pristine SnSe exhibits a discernible coherent phononic response, primarily governed by the A_g1 and $A_g{}^2$ modes. The observed behavior is well-described by a combination of two damped harmonic oscillators, facilitating the analysis of the frequencies (31.4, 69.4 cm^{-1}) and lifetimes (6.1, 3.5 ps), of the phonon modes (see details in Figure S1, Supporting Information), the results of which agree well with the literature[27] and the Raman measurements. This further confirms the formation of high symmetry phases in these samples. Electron

Y. Zhu, M. Liu, J. Sui
National Key Laboratory for Precision Hot Processing of Metals
Harbin Institute of Technology
Harbin 150001, China
O. Cojocaru-Mirédin
INATECH
Albert Ludwigs University of Freiburg
79110 Freiburg, Germany
M. Wuttig
Peter Grünberg Institute, JARA-Institut Energy-efficient information technology (PGI-10)
Forschungszentrum Jülich GmbH
52428 Jülich, Germany

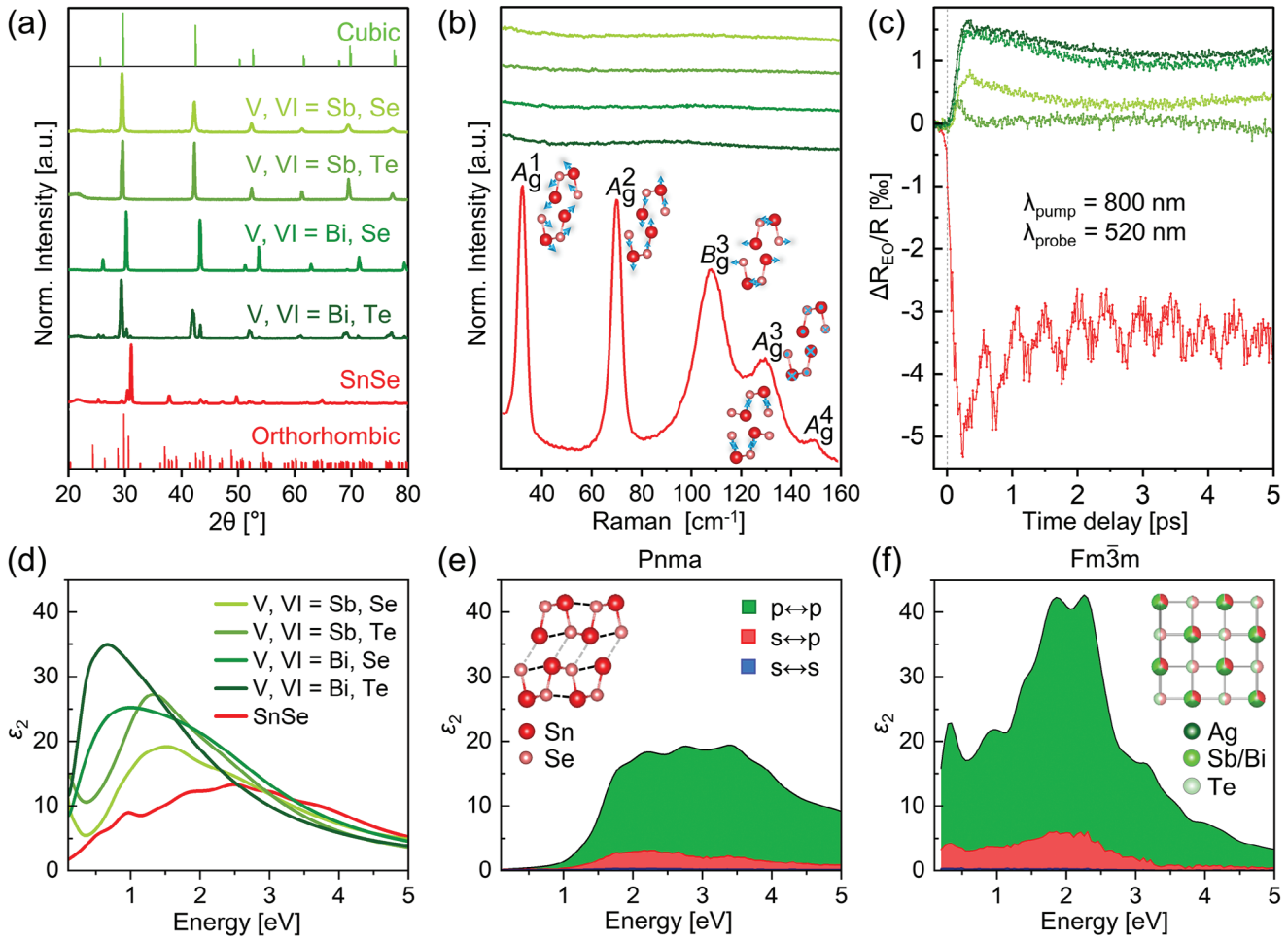

Figure 1. a) Powder XRD patterns for pure SnSe, $(SnSe)_{0.67}(AgBiTe_2)_{0.33}$, $(SnSe)_{0.67}(AgBiSe_2)_{0.33}$, $(SnSe)_{0.67}(AgSbTe_2)_{0.33}$, and $(SnSe)_{0.5}(AgSbSe_2)_{0.5}$ samples at room temperature. The standard cubic and orthorhombic phases of SnSe can refer to ICSD_CollCode12863 and ICSD_CollCode76032, respectively. b) Raman spectra for these SnSe samples. c) Transient reflectance data, obtained by pump-probe spectroscopy, in the EO scheme. Only the pristine SnSe sample shows significant oscillations due to lattice vibrations. These can be attributed to the Raman-active A_g^1 and A_g^2 phonon modes. d) The imaginary part of the dielectric function for pristine *Pnma* and *Fm*$\bar{3}$*m* SnSe alloys obtained from Kramers–Kronig transformation of the experimentally measured optical reflectivity data, with the Drude contribution being subtracted. The orbital-resolved imaginary part of the dielectric function for e) *Pnma* SnSe and for f) *Fm*$\bar{3}$*m* SnSe.

backscattered diffraction (EBSD) also corroborates the homogeneous cubic structure of these SnSe–$AgVVI_2$ polycrystals, as shown in Figure S2 (Supporting Information). The phase transition from the orthorhombic to the cubic phase can be described in terms of a vanishing Peierls-like lattice distortion.[43] The arrangement of atoms in solids is determined by chemical bonds between the atoms, favoring the configuration with the lowest energy. To better understand the origin of different structures in pristine SnSe and alloyed SnSe samples, Fourier transform infrared spectroscopy (FTIR) and ultraviolet–visible spectroscopy (UV–vis) measurements were performed to investigate the optical properties, which are governed by the interband transition that changes dramatically with changes of bonding. The corresponding imaginary part of the dielectric constant (ϵ_2) as a function of photon energy is shown in Figure 1d. Pristine SnSe shows a broad absorption over a large energy range while the maximum value of ϵ_2 is only ≈13. In stark contrast, all alloyed samples show much stronger optical absorptions at lower energy with a ϵ_2 maximum higher than that of pristine SnSe. The orbital-resolved ϵ_2 as a function of photon energy for both pure *Pnma* and *Fm*$\bar{3}$*m* SnSe phases were calculated, as illustrated in Figure 1e,f, respectively. The trend visible in the calculated data is congruent with the experimental data, i.e., the cubic phase exhibits a much larger ϵ_2 maximum at lower energy. The responsible interband transition is dominated by p-bands of Sn and Se, while the interaction between Sn-s and Se-p bands is rather small for both structures. The maximum of ϵ_2 (E), i.e., $\epsilon_2^{max}(E)$, shifts to lower energies and increases in magnitude upon the transition from orthorhombic (*Pnma*) to cubic (*Fm*$\bar{3}$*m*). The much-improved optical absorption in the cubic phase is due to the increased p–p orbital overlap, which enlarges the matrix element for interband transition.[30,44] Alloying SnSe with cubic $AgVVI_2$ compounds increases the p–p interaction and thus drives the structural phase transition. The increasing degree of p–p bond alignment increases electron delocalization and thus changes chemical bonding,[30] leading to modifications in the transport properties, as discussed next.

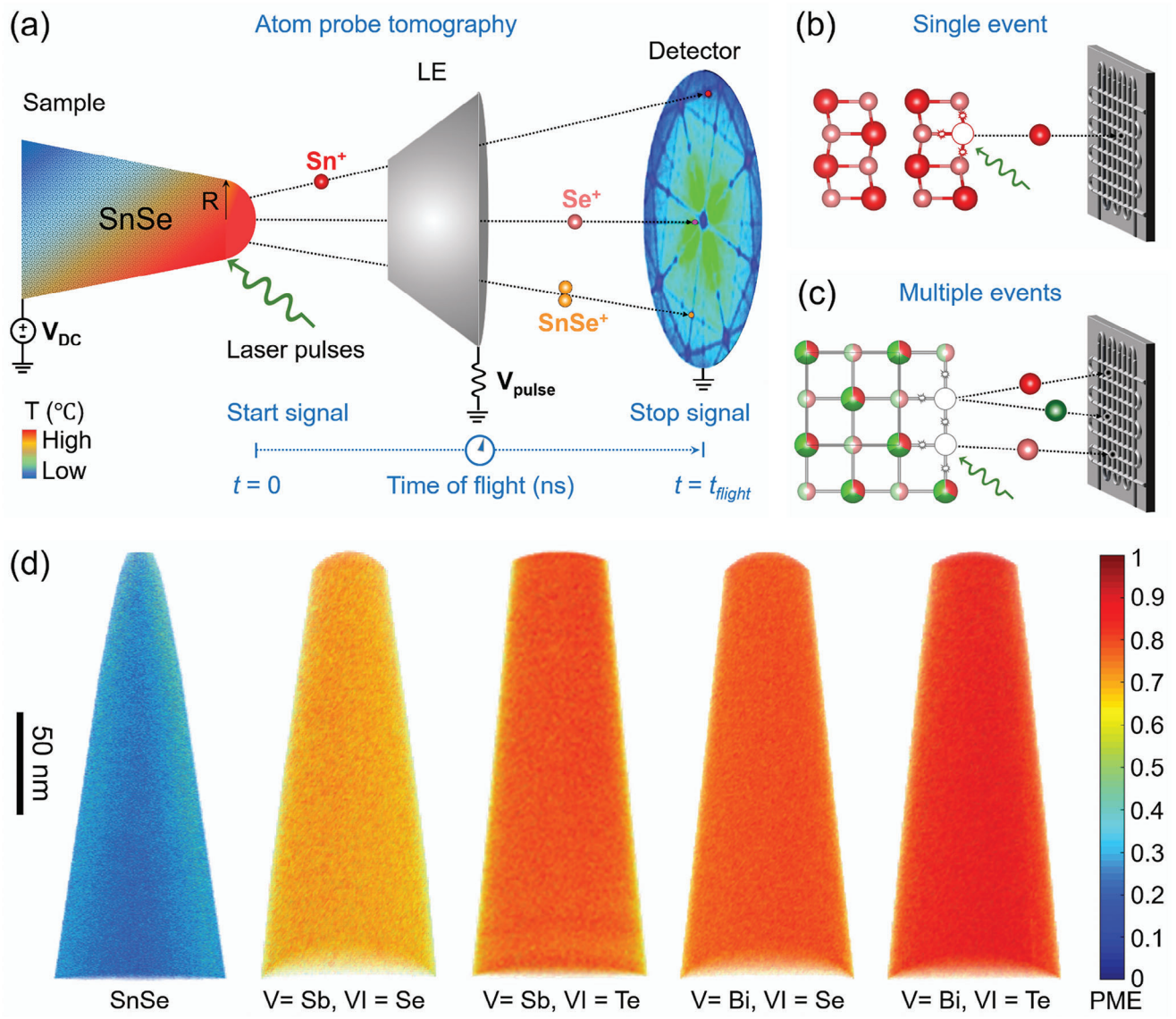

Figure 2. a) Schematic of laser-assisted atom probe tomography (APT). A needle-shaped specimen is illuminated by laser pulses, which effectively trigger the process of field evaporation. Schematic diagrams illustrate b) a single event and c) multiple events for the evaporation of ions with one successful laser pulse. d) PME of pristine SnSe and SnSe–$AgVVI_2$ alloys.

2.2. Chemical Bonding Mechanism Underpinning the Phase Transition

To characterize the accompanying bonding evolution upon the structural transition, atom probe tomography (APT) studies were conducted. **Figure** 2a sketches the important components and working principles of APT.[45–47] The surface atoms of a needle-shaped specimen are ionized in a high electric field and then evaporated toward a position-sensitive detector triggered by laser pulses. The evaporation behavior depends on the chemical bonding of specimens since the bonds are ruptured leading to atom desorption. Typically, a successful laser pulse dislodges only one ion from the specimen surface, called a "single event" (Figure 2b). Only a small fraction of laser pulses causes the evaporation of multiple ions within one successful pulse, referred to as "multiple events", as depicted in Figure 2c. A small but nonzero probability of multiple events (PME) is observed during APT measurements for the majority of materials.[48] Interestingly, a collection of solids has been found to show a bond-breaking process with an unconventionally high PME value.[47,49] These solids employ metavalent bonding (MVB) as revealed by their unique portfolio of properties including a large optical dielectric constant, a high Born effective charge (Z^*), and a large transverse optical mode Grüneisen parameter,[50–52] Figure 2d shows a low PME value (≈30%) for pristine SnSe, consistent with its covalent bonding nature. In striking contrast, all SnSe–$AgVVI_2$ alloys show high PME values ranging from 71% to 85% depending on their composition. Note that a high PME value larger than 60% is considered a hallmark of MVB, which has been demonstrated upon comparing ≈100 different compounds.[47,49,53,54] The

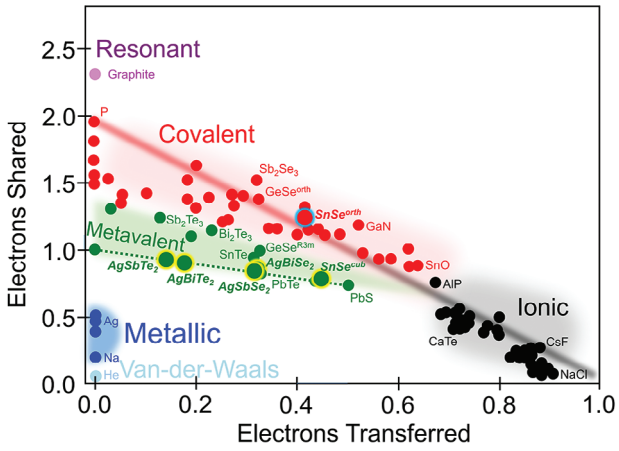

Figure 3. Illustrative diagram of the number of electrons transferred (*ET*), normalized by the oxidation state, as well as the number of electrons shared (*ES*) between neighboring atoms. The map effectively delineates several bonding mechanisms. The color of different solids is characteristic of the properties of different materials. The data presented in this figure have been obtained and modified from referenced sources,[30,55] except for the cubic ($Fm\bar{3}m$) SnSe phase, which has been calculated in this work.

mechanisms responsible for this high PME value are beyond the scope of this work. Instead, we only use the large PME as another accessible fingerprint of metavalent bonding. More details of APT measurements for these SnSe-based samples including the 3D distribution of constituting elements and 1D PME profile are provided in the supplementary information from Figures S3–S7 (Supporting Information). Overall, both composition and PME are homogeneous in the matrix of all samples.

Owing to the emergence of quantum–chemical calculation tools,[55] chemical bonding mechanism can be described by the number of electrons transferred (*ET*) and electrons shared (*ES*) between adjacent atoms, as shown in **Figure 3**. In the case of a pure ionic bond, the *ET* value, renormalized by the formal oxidation state of the atoms involved, is expected to be close to one. Conversely, a pure covalent bond is characterized by an *ES* value of two, approaching an electron pair proposed by Gilbert Lewis.[56] The majority of compounds reside around the connecting line between ionic and covalent bonds. The respective magnitudes of *ES* and *ET* serve as discerning indicators of the relative contributions of covalent and ionic bonding. Metallic bonding is found in the lower-left region, characterized by small or vanishing *ET* values and small *ES* values. These classic chemical bonding mechanisms can thus be quantified and displayed in a single map. More significantly, there is another group of materials in the map that is separate from the abovementioned bonding mechanisms. These solids show *ES* values of about one and small *ET* values, as demarcated in the green region in Figure 3. The compounds in this region exhibit distinctive properties, such as large optical dielectric constants (ϵ_∞), high Born effective charges (Z^*), and pronounced anharmonicity.[50,55] This unconventional combination of properties has not been found in materials utilizing metallic, covalent, and ionic bonding.[50] This leads to the designation of a unique bonding mechanism called metavalent bonding (MVB).[49,50,52] **Table 1** summarizes several property-based bonding indicators for pristine orthorhombic and cubic SnSe

Table 1. Property-based chemical bonding indicators for orthorhombic and cubic SnSe phases obtained by DFT calculations. The PME values are measured by APT. Since we could not stabilize the pure cubic SnSe phase at low temperatures, we used the PME values measured in cubic SnSe–$AgVVI_2$ alloys.

Type	ϵ_∞	ϵmax $_2$ (E)	Z^*	*ET*	*ES*	PME
$SnSe^{ortho.}$	11.6	17.2	3.4	0.41	1.24	30%
$SnSe^{cubic}$	35.3	37.4	6.4	0.43	0.79	71–85%

phases, confirming metavalent bonding in cubic SnSe. These two SnSe phases with different *ES* and *ET* values are also displayed in the bonding map, where *Pnma* SnSe is located in the covalent bonding region, while $Fm\bar{3}m$ SnSe is found in the MVB region. It is noteworthy that all the aforementioned $AgVVI_2$ compounds used to alloy with SnSe employ MVB, as highlighted by yellow circles in Figure 3. The orthorhombic SnSe structure can be derived from the cubic SnSe with a Peierls-like structural distortion. The degree of Peierls distortion directly depends on the *ES* value. Materials positioned on the dashed green line in Figure 3 possess a perfect octahedral arrangement without any Peierls distortion. Solids in the green region above the dashed line possess a Peierls distortion, which increases with increasing the *ES* value.[44] Concomitantly, the electrons will redistribute due to the formation of short and long bonds. While the short bonds become stronger, the long bonds become weaker,[55] which ultimately turn into covalent bonding and van der Waals-like or even true van der Waals bonding, respectively. Upon the bonding transition from metavalent to covalent (red region in the map), the degree of Peierls distortion is rather pronounced,[44] inducing a rearrangement of atomic positions to form an orthorhombic structure such as *Pnma* SnSe. On the contrary, reducing the degree of Peierls distortion will decrease the *ES* value from the red region to the green region on the map in Figure 3. At the same time, metavalent bonding also will collapse, if the charge transfer between adjacent atoms is too large. This happens if *ET* is too large. In our design, the alloying of strongly Peierls-distorted *Pnma* SnSe with distortion-free $AgVVI_2$ compounds (and small charge transfer) can increase the p–p orbital overlap, as confirmed by the optical absorption in Figure 1d, and thus lowers the degree of Peierls distortion. As a consequence, a cubic $Fm\bar{3}m$ SnSe alloy is formed due to the chemical bonding transition from covalent to MVB.

2.3. Improved Thermoelectric Performance in Metavalently Bonded Phases

The formation of the metavalent SnSe phase significantly influences the thermoelectric properties. **Figure 4a** compares the temperature-dependent electrical conductivity for SnSe–$AgVVI_2$ alloys with pristine polycrystalline SnSe, which has been taken from the literature.[19] Pristine SnSe shows a very poor electrical conductivity with 0.9 S cm^{-1} at room temperature. This extremely small electrical conductivity is mainly due to the intrinsically low charge carrier concentration (n), which is $\approx 2.0 \times 10^{17}$ cm^{-3}.[19] In contrast, the electrical conductivity increases by several orders of magnitude upon alloying with $AgVVI_2$ compounds. The differences among these alloyed samples are primarily due to the different chemical compositions that lead to slight changes in

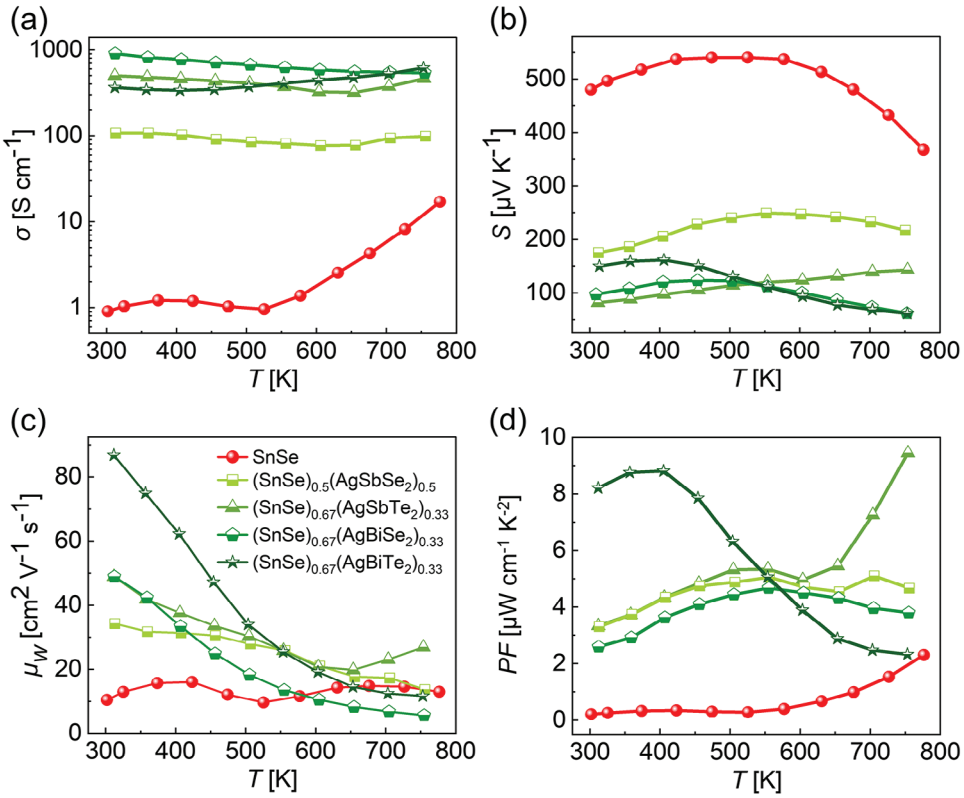

Figure 4. Temperature-dependent electrical transport properties of polycrystalline SnSe alloys. a) Electrical conductivity (σ) in a log scale. b) Seebeck coefficient (S). c) Weighted mobility (μ_W). d) Power factor (PF). The data for pristine SnSe taken from the literature[19] were measured along the direction of the SPS pressure.

carrier concentration and bandgap, see Table S1 (Supporting Information). The significant increase in Hall carrier concentration in the cubic SnSe alloys could be partly attributed to the much lower cation vacancy formation energy in cubic SnSe than that in the orthorhombic SnSe, as illustrated in **Figure 5**. This is consistent with the p-type semiconducting behavior in the cubic phase given the negative formation energy of Sn vacancies in both Sn-rich and Se-rich conditions. Due to the very demanding computation cost, we did not calculate the defect formation energy of the complex cubic alloys. Microstructure characterizations by energy dispersive spectroscopy (EDS) reveal the presence of Sb-rich or Ag-rich precipitates in these cubic alloys, as shown in Figures S8–S11 (Supporting Information). The formation of these precipitates leaves cation vacancies in the matrix, which lower the Fermi energy level and depopulate the antibonding states in metavalently bonded solids to stabilize the structure.[57] The low vacancy formation energy is in line with the soft chemical bonds of MVB as characterized by a bond order of 0.5 and strong lattice anharmonicity.[26,30] Thus, the energy required to remove one atom to form a vacancy in MVB solids is much lower than that in the covalently bonded counterpart.

The much-increased carrier concentration (n) will inevitably reduce the Seebeck coefficient (S) according to the Pisarenko relationship,[58,59] as expressed in Equation (1).

$$S = \frac{8\pi^2 k_B^2}{3eh^2} m^* T \left(\frac{\pi}{3n}\right)^{\frac{2}{3}} \quad (1)$$

where k_B, e, h, and m^* represent the Boltzmann constant, electron charge, the Planck constant, and density-of-states effective mass, respectively. Figure 4b shows huge Seebeck coefficients for pristine SnSe due to its large bandgap and low carrier concentration. In contrast, the Seebeck coefficients for cubic SnSe alloys are not far away from the optimum range.[60–62] Furthermore, they can be optimized by tuning the carrier concentration. There is a prominent drop in the Seebeck coefficient with temperature for the $AgBiTe_2$-alloyed sample above 400 K. This is due to the strong bipolar effect, which induces the intrinsic excitation of minority carriers, compensating for the Seebeck voltage generated by oppositely charged carriers. This bipolar effect is also observed in the temperature-dependent electrical conductivity in Figure 4a. Even though cubic SnSe alloys show high carrier concentrations of the order of 10^{20} cm^{-3}, the resulting Seebeck coefficients remain relatively large. This is indicative of a high density-of-states (DOS) effective mass (m^*) for the cubic alloys as described in Equation 1 and listed in Table S1. The pristine SnSe embraces a m^* value of 0.43 m_e calculated according to the single parabolic band model (m_e is the free electron mass),[63] which is in line with the value measured by angle-resolved photoemission spectroscopy.[64] In contrast, the m^* values for cubic SnSe alloys are significantly larger than those of the pristine SnSe. Yet, a large effective mass is often detrimental to the carrier mobility, which degrades the electrical conductivity.[65] Thus, the power factor ($PF = S^2\sigma$) depends on the tradeoff between the DOS effective mass and the carrier mobility given that the carrier concentration

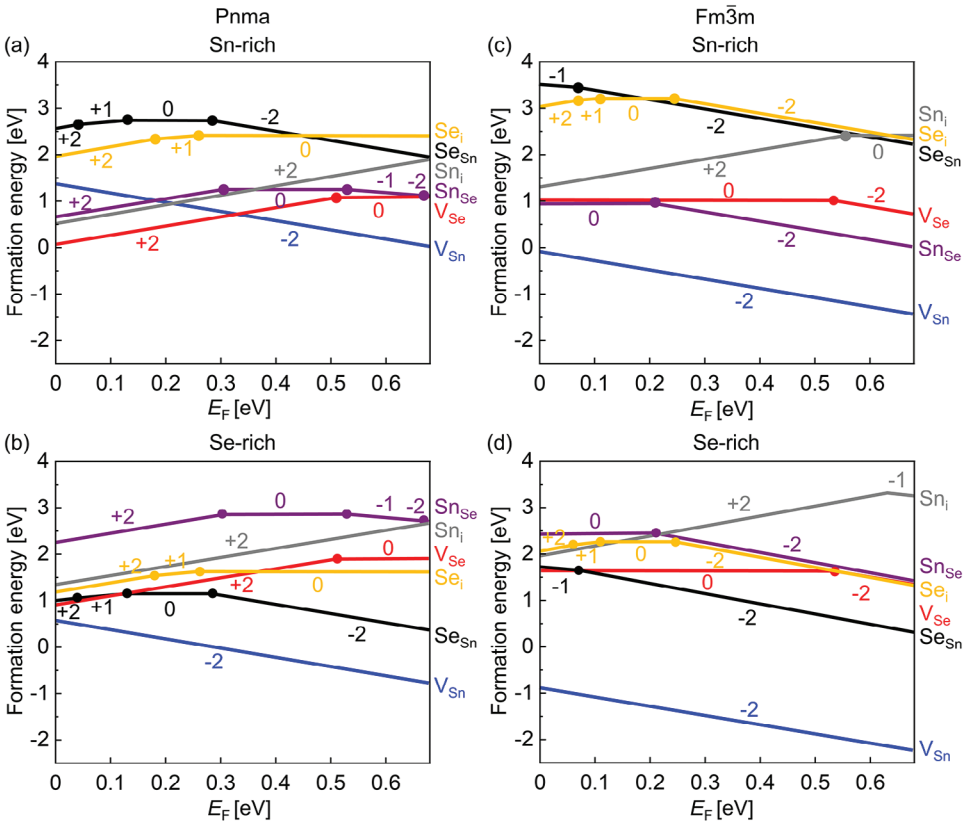

Figure 5. The formation energy of different defects for *Pnma* SnSe at a) Sn-rich, b) Se-rich, and for *Fm*$\bar{3}$*m* SnSe at c) Sn-rich and d) Se-rich conditions.

has been optimized. This relationship can be expressed by the weighted mobility (μ_W),[66] i.e., the carrier mobility weighted by the DOS effective mass, as shown in Equation (2).

$$\mu_W \approx \mu\left(\frac{m^*}{m_e}\right)^{\frac{3}{2}} = \mu N_V\left(\frac{m_b^*}{m_e}\right)^{\frac{3}{2}} \quad (2)$$

where m_b^* is the band effective mass and N_V is the valley degeneracy. Figure 4c shows the temperature-dependent weighted mobility values calculated using experimental electrical conductivities and Seebeck coefficients following the method described by Snyder et al.[67] Pristine polycrystalline SnSe sample shows two "up and down" trends in the weighted mobility curve. The first increase up to 400 K can be described as a thermally-activated conduction process due to the charge carrier scattering at grain boundaries.[21,68–70] The second increase from 500 to 700 K is induced by the continuous phase transition from *Pnma* to *Cmcm* symmetry. All other cubic SnSe samples show a decreasing trend in the weighted mobility with rising temperature, indicative of a metal-like or degenerate semiconducting behavior. This also implies that the charge carrier scattering at grain boundaries in cubic SnSe samples is much weaker than that in pristine SnSe. Since pristine SnSe utilizes covalent bonding, while the cubic SnSe samples employ metavalent bonding, the static dielectric constant for the cubic samples is much larger than that for the covalent phase according to the Lyddane–Sachs–Teller relation.[69] As a result, the weaker charge carrier scattering at grain boundaries in the MVB phases can be attributed to the dielectric screening effect.[71] The much-improved weighted mobility for the cubic SnSe alloys leads to higher power factors over a wide temperature range compared with pristine SnSe (Figure 4d). We also compared the electronic quality factor (B_E)[62] and intrinsic conductivity (σ_0)[61] between these SnSe polycrystals, as shown in Figure S12 (Supporting Information). The results are in line with the weighted mobility analyses confirming that cubic SnSe alloys possess better electrical performance. In particular, with the introduction of 33% $AgBiTe_2$ into SnSe, the power factor is boosted approximately nine times from 0.9 μW cm^{-1} K^{-2} for pristine SnSe to 8.0 μW cm^{-1} K^{-2} for the alloyed sample at 300 K. This value is among the highest reported so far around room temperature in polycrystalline SnSe compounds.[19–22,35,70,72] A high room-temperature power factor has also been observed in the p-type cubic pure SnSe phase under high pressure.[73] The increased average power factor is favorable for larger power output performance.[74] On the contrary, a relatively high power factor in the pristine polycrystalline SnSe sample can only be achieved at high temperatures when the high-symmetry *Cmcm* SnSe phase dominates. Note that the same MVB mechanism of these cubic SnSe alloys does not necessarily lead to exactly the same properties for all MVB solids. As can be seen in Figure 3, different chemical bonding mechanisms spread over a large area on the map spanned by two quantum–chemical variables, i.e., the electrons transferred (*ET*) and the electrons shared (*ES*). The *ET* and *ES* are not only chemical bonding descriptors but also excellent material property predictors, due to the close

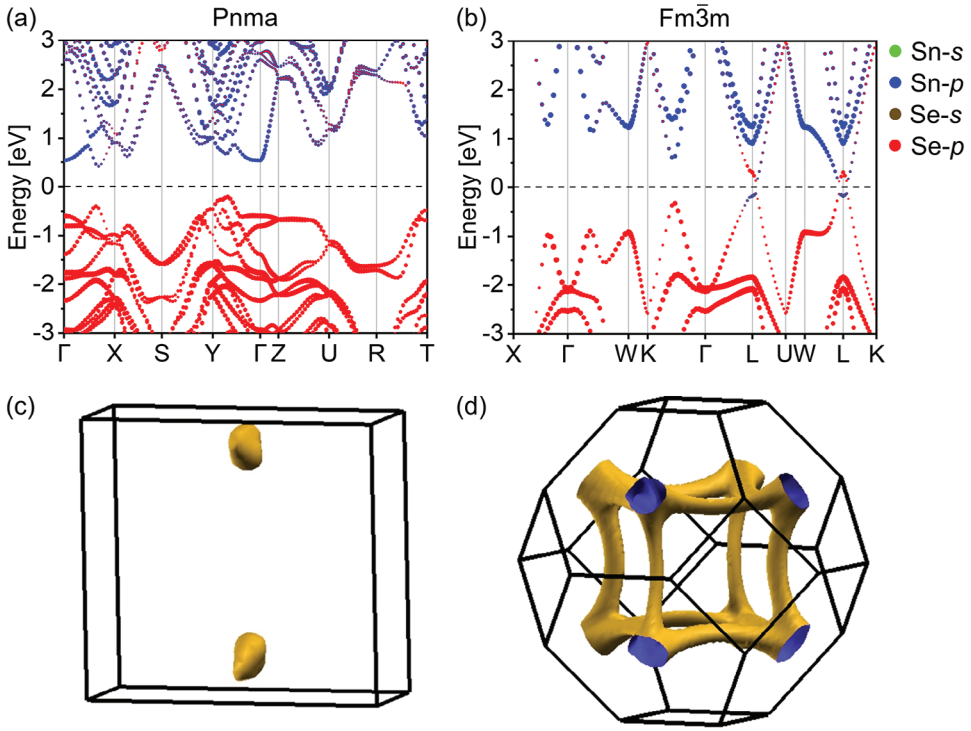

Figure 6. Electronic band structures for different SnSe phases were calculated by including the spin-orbital coupling effect. a) *Pnma* SnSe; b) *Fm*$\bar{3}$*m* SnSe. Corresponding constant energy surfaces at the value of −0.3 eV and −0.4 eV relative to the Fermi energy in the first Brillouin zone for c) *Pnma* SnSe and d) *Fm*$\bar{3}$*m* SnSe phases, respectively.

relationship between chemical bonding and resulting material properties.[51] For example, the *ET* value increases from PbTe to PbSe and then to PbS due to the increased ionicity, leading to the decreased maximum power factor along this line.[30] Due to the high computation cost for complex materials, we only calculated the *ES* and *ET* values for pure SnSe phases. These values might be different for different SnSe–AgVVI$_2$ alloys, which are responsible for the different thermoelectric properties. Nevertheless, the thermoelectric performance of these MVB solids is in general much higher than that of the covalently bonded SnSe.

Figure 6a,b display the orbital-resolved band structures of orthorhombic and cubic SnSe, as determined by DFT calculations including the spin-orbital coupling effect (details are described in the Methods section). The conduction and valence bands near the Fermi energy are dominated by the p states of Sn and Se, respectively, supporting the idea that the significance of s-lone pairs for electrical transport may not be as pronounced as previously believed, as also exemplified in an IV–VI compound PbTe.[75] This is consistent with our optical absorption data, which shows that the interband transition primarily occurs between p states. The *Pnma* phase has a bandgap of 0.63 eV, in line with experimental data and other calculations.[4] In comparison, the pure *Fm*$\bar{3}$*m* SnSe phase shows a small bandgap of 0.24 eV. This value is in line with the experimental bandgaps of cubic SnSe–AgVVI$_2$ alloys in the range of ≈0.12–0.28 eV calculated according to the Goldsmid–Sharp method[76] as listed in Table S1 (Supporting Information) and DFT calculations in the literature.[77] Even though the complex compositions of alloys were not included in our DFT calculations, the electronic band structure of the pure cubic SnSe phase should still represent some key features of the cubic alloys, such as the m_b^* and the valley degeneracy. The m_b^* of the valence band for the orthorhombic and cubic SnSe phases determined by DFT calculations is 0.25 m_e and 0.09 m_e, respectively, in line with literature data.[78] The reduced m_b^* in the cubic phase can be ascribed to the enhanced p–p orbital overlap, which creates a larger band dispersion. Figure 5c shows the constant energy surfaces at a value of 0.3 eV below the Fermi energy in the first Brillouin zone for the *Pnma* SnSe phase, which indicates a valley degeneracy (N_V) of 2. In stark contrast, the cubic phase possesses many equivalent symmetry points in the Brillouin zone, leading to increased valley degeneracy. The energy difference between the L and Σ points in the cubic *Fm*$\bar{3}$*m* SnSe phase is only 0.2 eV as determined in Figure 6b. The Fermi energy can cross both bands with proper chemical doping, resulting in the band convergence effect. Thus, the cubic phase has a total valley degeneracy (N_V) of 16 with 4 from the L point and 12 contributed by the Σ point. Note that a value of 0.4 eV below the Fermi energy was used in Figure 6d to better visualize the constant energy surfaces. The large N_V value is the dominant cause of the improved weighted mobility and power factor in cubic SnSe alloys.

Figure 7a shows the total thermal conductivity (κ_{tot}) as a function of temperature. The relevant parameters including the sample density (ρ), the specific heat (C_p), and the thermal diffusivity (D) are displayed in Table S1 and Figure S13 (Supporting Information). Since the total thermal conductivity consists of contributions from the lattice vibration (κ_{lat}), heat-carrying charge carriers (κ_{ele}), and bipolar heat conduction, the increased κ_{tot} in cubic SnSe alloys is mainly induced by the substantially increased

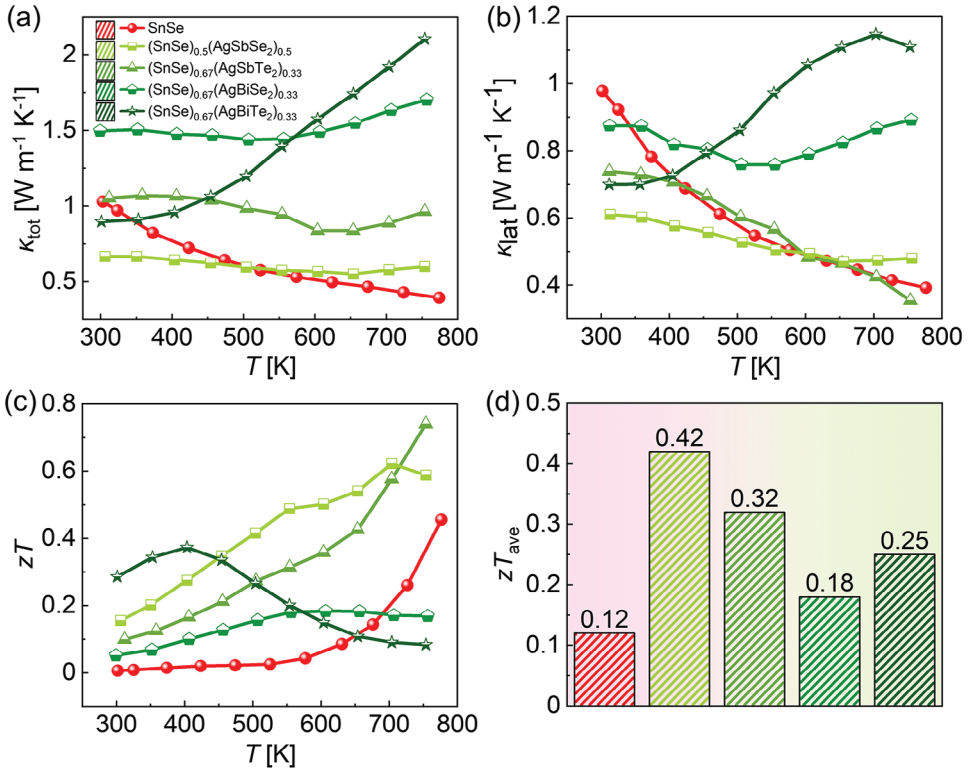

Figure 7. Temperature-dependent thermal transport properties and figure of merit (zT) of $AgVVI_2$ alloyed SnSe samples. a) total thermal conductivity (κ_{tot}). b) lattice thermal conductivity, κ_{lat}. c) thermoelectric figure of merit zT ($zT = S^2\sigma T/\kappa_{tot}$), and d) average zT value (zT_{ave}) over the whole temperature range measured. The data for pristine SnSe taken from the literature[19] were measured along the direction of the SPS pressure.

electrical conductivity. The electronic thermal conductivity can be calculated based on Wiedemann Franz's law, $\kappa_{ele} = L\sigma T$, where the Lorenz number (L) is derived using a single parabolic band (SPB) model (L and κ_{ele} are provided in Figure S9, Supporting Information).[79,80] By subtracting κ_{ele} from κ_{tot}, the κ_{lat} obtained is shown in Figure 7b. Note that this value also includes the contribution from the bipolar effect. The lattice thermal conductivity of all alloyed samples is lower than that of pristine SnSe near room temperature when the bipolar effect is not pronounced. The significant increase in κ_{lat} with temperature for samples SnSe–$AgBiSe_2$ and SnSe–$AgBiTe_2$ is due to the bipolar heat conduction. The lowered lattice thermal transport upon alloying with $AgVVI_2$ comes from several aspects. First, the soft metavalent bonds result in a lower phonon group velocity.[26] Second, the delocalized p-electrons in MVB can strongly couple with the transverse optical phonons, lowering the phonon frequency and increasing the anharmonicity.[81] Third, the alloying elements increase the complexity of atomic arrangements, enhancing the scattering strength of phonons by point defects.[82] All these factors give rise to the reduction of lattice thermal conductivity.

Owing to the enhanced power factor ($S^2\sigma$) across a broad temperature range and the reduced lattice thermal conductivity near room temperature, the final zT values of cubic SnSe alloys are improved compared to pristine SnSe (Figure 7c). An abrupt increase in zT for pristine SnSe is only observed above 650 K, where a more symmetric *Cmcm* phase dominates.[83] DFT calculations have shown evidence for the existence of metavalent bonding in the *Cmcm* phase of SnSe.[84,85] Yet, experimentally proving the MVB mechanism of *Cmcm* SnSe only seems feasible if this phase can be stabilized at ambient conditions, which is still a big challenge. In the temperature range of 300–750 K, the average zT (zT_{ave}) of all MVB SnSe–$AgVVI_2$ alloys is greater than that of pristine covalent SnSe, as illustrated in Figure 7d. The zT values of cubic SnSe–$AgVVI_2$ alloys obtained in this work are comparable to those reported in the literature[35,39,86] given the standard measurement error of ≈20% for zT. Further enhancement of zT can be achieved by introducing extra dopants such as Pb[35] and Ge[39] in the cubic system to meticulously tune the ES and ET values as well as microstructural defects.

3. Conclusion

We demonstrate that the high-symmetry cubic SnSe phase shows higher thermoelectric performance than its low-symmetry *Pnma* counterpart. The structural transition can be manipulated by tailoring the chemical bonding mechanism. A stronger optical absorption is observed in the cubic phases due to the increased p–p orbital overlap. In addition, these cubic phases show a large optical dielectric constant, a high Born effective charge, and abnormal bond-breaking behavior with a high "probability of multiple events". This combination of properties verifies the metavalent bonding mechanism in cubic SnSe alloys. In contrast, the pristine *Pnma* SnSe utilizes covalent bonding. Owing to the formation of metavalent bonds, the power factor of the cubic SnSe phase is significantly improved mainly due to the increase in carrier concentration and valley degeneracy. The soft metavalent

bonds in conjunction with alloy scattering to phonons also lead to a low thermal conductivity. As a consequence, the zT value of polycrystalline cubic SnSe solids at low temperatures is improved by a factor of more than 10 compared to pristine *Pnma* SnSe. This strategy of manipulating the structure symmetry and thermoelectric performance by tailoring chemical bonds can also be extended to other chalcogenides such as SnS and GeS.

4. Experimental Section

Sample Preparation: High-purity Sn (99.999%), Ag (99.9%), Sb (99.999%), Se (99.999%), and Te (99.999%) shots were weighed according to the atomic ratio of $(SnSe)_{0.67}(AgBiTe_2)_{0.33}$, $(SnSe)_{0.67}(AgBiSe_2)_{0.33}$, $(SnSe)_{0.67}(AgSbTe_2)_{0.33}$, and $(SnSe)_{0.5}(AgSbSe_2)_{0.5}$. The raw materials were sealed in quartz tubes under a high vacuum ($\approx 10^{-5}$ mbar) and melted in a muffle furnace at 1223 K for 40 h. The samples were furnace-quenched and ground to fine powders with a mortar and pestle in an Argon-filled glove box, then transferred to a graphite sintering mold with an inner diameter of 20 mm for sintering. The powders were then sintered at a maximum temperature of 873–923 K for 5 min under an axial pressure of 50 MPa using spark plasma sintering (SPS, FCT Systeme GmbH) with the pyrometer temperature control mode.

Powder X-ray Diffraction: The stoichiometry and phase of the crystals were checked on a Bruker D8 Discover diffractometer with Cu Kα radiation ($\lambda = 1.5406$ Å) using a Bragg–Brentano geometry and a LYNXEYE detector in 1D mode. Fine powders for X-ray diffraction were obtained by grinding the crystal ingots and then sieved into particles of $\approx$30 µm.

Scanning Electron Microscopy (SEM) and Energy Dispersive Spectroscopy (EDS): These measurements were carried out using a dual-beam SEM/focused ion beam (FIB, Helios NanoLab 650, FEI) equipped with an Oxford silicon drift detector. The acceleration voltage and current for EDS measurements were 20 kV and 1.6 nA, respectively. The data collection and analyses were processed using the Aztec Energy analysis software.

Raman Spectroscopy Measurements: The Raman spectroscopy measurements were conducted with a commercial WITec system (alpha300), operating in backscattering geometry. A diode-pumped solid-state laser supplied linearly polarized light with a wavelength of 532 nm (2.33 eV). This was delivered through a single-mode optical fiber and used to excite the sample. The spot size of 400–500 nm was obtained by employing a long working focusing lens with a numerical aperture of 0.70. By setting the excitation power to 500 µW, significant heating effects were avoided. For detection, the reflected light was delivered through a single-mode optical fiber to a charge-coupled spectrometer with a grating of 2400 lines per mm. All measurements were obtained at room temperature with a 50×(NA = 0.7) objective.

Optical Measurements: Reflectance measurements in the spectral range of 15–18000 cm^{-1} were conducted using a Bruker Vertex 80v Fourier-transform spectrometer. A 200 nm thick gold mirror served as a reference. Multiple sources (Hg-arc, globar, and tungsten lamp), beam splitter (Mylar 50 µm, multilayer, KBr, and CaF_2), and detector (liquid He-cooled 4K silicon bolometer, DLaTGS (one with polyethylene and the one with KBr window), liquid nitrogen-cooled InSb and room-temperature Si photodiode) combinations were utilized to cover the entire spectral range. An Avantes AvaSpec-2048CL-EVO spectrometer and an aluminum reference mirror were used for the measurement of reflectance in the 9100–45000 cm^{-1} spectral range. By employing Kramers–Kronig analysis and utilizing X-ray atomic scattering functions for extrapolation at high energy, the real and imaginary parts of the optical dielectric functions (ϵ_1(E), ϵ_2(E)) were derived from the reflectivity data. The procedures to obtain the complex dielectric functions from the reflectance data are given in the Supporting Information.

Femtosecond Pump-Probe Reflectivity Measurements: The study employed a two-color pump-probe experiment, utilizing both isotropic and anisotropic arrangements for ultrafast optical measurements. All data shown in the main article were obtained via anisotropic sampling. A Ti:Sapphire regenerative femtosecond amplifier producing 800 nm pulses with a 60 fs width was used in the setup. The pump beam, chopped at 1500 Hz, was decoupled and directed through an optical delay line before focusing on the sample (200 µm diameter spot size). The probe pulses were frequency converted to 520 nm using an optical parametric amplifier, with a resulting pulse width of 70 fs, and were focused to a 30 µm spot on the sample. To facilitate the material response detection, two balanced Si-photodiodes were connected to variable gain current amplifiers and a data-acquisition card. All measurements were performed at the same pump fluency, at the order of 1 mJ cm^{-2}, while the probe fluency was smaller by a factor of 10. The reflected probe beam was split into its s- and p-polarized components by a polarizing beam splitter cube. Both isotropic and anisotropic transient reflectance data were normalized to steady-state reflectance (R_0), obtained when the pump pulse was chopped. For isotropic sampling, the transient reflectance (ΔR) was determined by combining the s- and p-polarized components of the reflected light.

$$\Delta R = \Delta(R_s + R_0)/R_0 \tag{3}$$

For the anisotropic measurements, an electro–optic detection scheme[42] was employed to calculate ΔR_{EO} from the s- and p-polarized components.

$$\Delta R_{EO} = \Delta(R_s - R_0)/R_0 \tag{4}$$

To ensure the reversibility of the optical excitation, the static reflectivity was monitored.

Atom Probe Tomography: Needle-shaped specimens were prepared using the SEM-FIB dual beam focused ion beam (Helios NanoLab 650, FEI) following the standard "lift-out" method.[87] APT measurements were performed on a LEAP 4000X Si instrument (CAMECA) using a UV laser ($\lambda = 355$ nm) with a laser pulse energy of 5–10 pJ. The pulse repetition rate was set at 200 kHz, and the specimen base temperature was maintained at 40 K. The average detection rate was 1.0%, and the ion flight path length was 160 mm. The APT data reconstruction was carried out using the commercial software IVAS 3.8 and home-coded software EPOSA.[88]

Thermoelectric Property Measurement: Samples in the bar shape with sizes $\approx 2 \times 2 \times 10$ mm were used for measuring the electrical conductivity and the Seebeck coefficient in a LINSEIS LSR-3 Seebeck machine. The Hall carrier concentrations (n_H) and Hall mobility (μ_H) were calculated by the formula of $n_H = 1/(eR_H)$ and $\mu_H = \sigma/(en_H)$, where the R_H is the Hall coefficient detected by the van der Pauw method with ±.5 T magnetic field. The total thermal conductivity was calculated as a product of $\kappa_{tot} = DC_p\rho$. The thermal diffusivity (D) and the mass density (ρ) were measured by a laser flash machine (LINSEIS LFA-1000) and an Archimedes kit, respectively. The specific heat (C_p) was calculated using the Dulong–Petit law. The uncertainty for electrical conductivity, Seebeck coefficient, and thermal conductivity were ≈4%, 5%, and 12%, respectively. In particular, the thermal conductivity uncertainty comprised 4% for thermal diffusivity, 6% for specific heat, and 2% for mass density. As a result, the combined uncertainty for the power factor and zT were 10% and 20%, respectively. For improved readability, error bars were been included in the curves of the presented figures in this article.

Density Functional Theory (DFT) Calculations: Projector-augmented wave (PAW) potentials[89] were used to calculate bond descriptors, electrons shared (*ES*), and transferred (*ET*). The DGRID[90] and Critic2 codes[91] were used to calculate the *ES* and *ET* values using Bader basins.[92] Integrating over the electron density of a singular Bader basin yields the electron population of the atom corresponding to the respective basin. The *ES* values were obtained by integrating over the exchange–correlation hole over the Bader basins of two atoms respectively. By subtracting the nominal charge of an atom from the electron population, and dividing the results by the formal oxidation state, *ET* was calculated.

First-principles calculations were based on the Vienna Ab initio Simulation Package (VASP).[93] The interaction between ions and valence electrons was described by Projected Augmented Wave (PAW),[89] and the exchange–correlation interaction was described by the Perdew–Burke–Ernzerhof generalized gradient approximation (PBE-GGA).[94,95]

The cutoff energy was set as 400 eV, and the convergence criteria for self-consistent electronic energy and residual force were respectively assumed to be 10^{-4} eV per atom and 0.01 eV $Å^{-1}$, respectively, which could ensure sufficient accuracy. The K points were set 6 × 6 × 2 and 4 × 4 × 4 based on Monkhourst–Pack meshes for SnSe in the *Pnma* and *Fm*$\bar{3}$*m* phases, respectively. For band structure calculations, the spin-orbital coupling effect was included and the paths of the Brillouin zone were set up based on previous work,[96] and the results of the band gaps were obtained by using the VASPKIT.[97] The visualization of the Fermi surface was performed using Xcrysden software.[98]

Defect Formation Energy Calculation: For SnSe in the *Pnma* and *Fm*$\bar{3}$*m* phases, the defect formation energies were calculated for 1 × 3 × 3 and 2 × 2 × 2 supercells containing 72 and 64 atoms, respectively. The cutoff energy was set as 350 eV, and the convergence criteria for self-consistent electronic energy and residual force as the same as band structure calculation. The k points were set 3 × 3 × 3 and 2 × 2 × 2 based on Monkhorst–Pack meshes. The optimized supercell showed lattice parameters of a = 11.68 Å, b = 4.21 Å, c = 4.53 Å, a = b = c = 6.06 Å, respectively, which were in good agreement with the experimental observations. To accurately calculate the total energies of the charged defect-containing models, the correction terms including potential alignment and the image charge were included to minimize the considerable supercell finite-size effects.[99]

The formation energy ($\Delta H_{D,q}$) of defect (D) in the charge state q was defined by Equation (5):

$$\Delta H_{D,q}\ (E_F, \mu) = E_{D,q} - E_H - \sum n_a \mu_a + q\,(E_F + E_V + \Delta V) \tag{5}$$

where $E_{D,q}$ and E_H are the total energies of the supercell with the defects in the charge state q and a perfect host supercell, respectively. n_a is the number of exchanged atoms (α) added to ($n_a > 0$) or removed from ($n_a < 0$) the defect supercell system, and μ_a is the corresponding chemical potential of the exchanged atoms (α). E_F is the Fermi level, and E_V corresponds to the VBM, which was corrected by the ΔV method.[100] This equation shows that the formation energy of the defects is a function of Fermi energy and the chemical potential of reactants.

For the calculations of defect formation energies, two different preparation conditions were simulated for these intrinsic defects, including Sn-rich (Se-poor) and Se-rich (Sn-poor). First, the chemical potential of Sn or Se must be less than its natural phase to avoid the formation of Sn (Equation 6) or Se (Equation 7) crystal.

$$u_{Sn} - {u_{Sn}}^0 < 0 \tag{6}$$

$$u_{Se} - {u_{Se}}^0 < 0 \tag{7}$$

where u^0_{Sn} (−3.82 eV) and u^0_{Se} (−3.31 eV) were the reference energies of Sn or Se crystal. Note that the growth of SnSe should satisfy the following thermodynamic equilibrium condition given by Equation (8):

$$\mu_{SnSe} = \mu_{Sn} + \mu_{Se} = -8.24 \text{ eV} \tag{8}$$

For SnSe, another phase of $SnSe_2$ tended to grow effectively under Se-rich growth conditions. To inhibit the formation of $SnSe_2$, the growth conditions must be restricted below the upper limit value of u_{Se}. In thermodynamic equilibrium for $SnSe_2$, the chemical potentials of Sn and Se atoms must satisfy the following constraint condition given by Equation (9):

$$\mu_{SnSe_2} = \mu_{Sn} + 2\,\mu_{Se} = -11.84 \text{ eV} \tag{9}$$

By inputting the calculated energies of the supercell with and without defects into Equations (5)–(9), the energy formation of the defects could be explicitly solved.

Supporting Information

Supporting Information is available from the Wiley Online Library or from the author.

Acknowledgements

N.L. acknowledges financial support from the China Scholarship Council (CSC). T. Ghosh acknowledges a postdoctoral fellowship from the Alexander von Humboldt Foundation. F. Hoff, T. Schmidt, and M. Wuttig acknowledge financial support from NeuroSys as part of the initiative "Clusters4Future", which is funded by the Federal Ministry of Education and Research BMBF (03ZU1106BA). The authors acknowledge the computational resources granted from RWTH Aachen University under project p0020357. Y. Zhou, Y. Yang, and P. Kerres from the Institute of Physics (IA) of RWTH Aachen University are greatly acknowledged for their helpful discussions.

Open access funding enabled and organized by Projekt DEAL.

Conflict of Interest

The authors declare no conflict of interest.

Author Contributions

N.L. and S.H. contributed equally to this work. Y.Y. conceived this project and wrote the manuscript. Y.Y. and M.W. supervised this project. N.L., P.Y., and R.H. prepared the samples. R.H. measured the thermoelectric properties. T.G. performed FTIR measurements and provided important suggestions and discussions about the manuscript. S.H. and C.Z. calculated the electronic band structures and defect formation energy. C-F.S. and D.K. calculated the ES-ET map and optical properties. J.F. performed the Raman measurement and data analysis. J.F. and F.H. performed the pump-probe measurement and data analysis. T.S. helped with the FTIR data processing. Y.Z., M.S., M.L., and J.S. carried out the Hall measurements. M.H. measured and analyzed XRD data. N.L. prepared the figures. O.C.-M., C-F.S., R.H., and M.W. commented on the manuscript. All authors approved the submission of this manuscript.

Data Availability Statement

The data that support the findings of this study are available from the corresponding author upon reasonable request.

Keywords

materials design, metavalent bonding, phase transition, SnSe alloys, thermoelectric materials

Received: December 8, 2023
Revised: March 24, 2024
Published online: April 4, 2024

[1] L. D. Zhao, S. H. Lo, Y. Zhang, H. Sun, G. Tan, C. Uher, C. Wolverton, V. P. Dravid, M. G. Kanatzidis, *Nature* **2014**, *508*, 373.
[2] P.-C. Wei, S. Bhattacharya, J. He, S. Neeleshwar, R. Podila, Y. Y. Chen, A. M. Rao, *Nature* **2016**, *539*, E1.
[3] P.-C. Wei, S. Bhattacharya, Y.-F. Liu, F. Liu, J. He, Y.-H. Tung, C.-C. Yang, C.-R. Hsing, D.-L. Nguyen, C.-M. Wei, M.-Y. Chou, Y.-C. Lai, T.-L. Hung, S.-Y. Guan, C.-S. Chang, H.-J. Wu, C.-H. Lee, W.-H. Li, R. P. Hermann, Y.-Y. Chen, A. M. Rao, *ACS Omega* **2019**, *4*, 5442.

[4] Z.-G. Chen, X. Shi, L.-D. Zhao, J. Zou, *Prog. Mater. Sci.* **2018**, *97*, 283.
[5] L.-D. Zhao, G. Tan, S. Hao, J. He, Y. Pei, H. Chi, H. Wang, S. Gong, H. Xu, V. P. Dravid, C. Uher, G. J. Snyder, C. Wolverton, M. G. Kanatzidis, *Science* **2016**, *351*, 141.
[6] C. Chang, M. Wu, D. He, Y. Pei, C.-F. Wu, X. Wu, H. Yu, F. Zhu, K. Wang, Y. Chen, L. Huang, J.-F. Li, J. He, L.-D. Zhao, *Science* **2018**, *360*, 778.
[7] B. Qin, D. Wang, X. Liu, Y. Qin, J.-F. Dong, J. Luo, J.-W. Li, W. Liu, G. Tan, X. Tang, J.-F. Li, J. He, L.-D. Zhao, *Science* **2021**, *373*, 556.
[8] L. Su, D. Wang, S. Wang, B. Qin, Y. Wang, Y. Qin, Y. Jin, C. Chang, L.-D. Zhao, *Science* **2022**, *375*, 1385.
[9] D. Liu, D. Wang, T. Hong, Z. Wang, Y. Wang, Y. Qin, L. Su, T. Yang, X. Gao, Z. Ge, B. Qin, L.-D. Zhao, *Science* **2023**, *380*, 841.
[10] L. Zhou, Y. Chen, R. Zhang, S. Zhao, X. Bai, M. Jin, *J. Inorg. Mater.* **2021**, *36*, 313.
[11] D. Feng, Y.-X. Chen, L.-W. Fu, J. Li, J.-Q. He, *Rare Met.* **2018**, *37*, 333.
[12] J. Li, J. Xu, H. Wang, G.-Q. Liu, X. Tan, H. Shao, H. Hu, J. Jiang, *J. Mater. Sci.: Mater. Electron.* **2018**, *29*, 18727.
[13] E. K. Chere, Q. Zhang, K. Dahal, F. Cao, J. Mao, Z. Ren, *J. Mater. Chem. A* **2016**, *4*, 1848.
[14] S. Sassi, C. Candolfi, J. B. Vaney, V. Ohorodniichuk, P. Masschelein, A. Dauscher, B. Lenoir, *Mater Today Proc* **2015**, *2*, 690.
[15] C.-L. Chen, H. Wang, Y.-Y. Chen, T. Day, G. J. Snyder, *J. Mater. Chem. A* **2014**, *2*, 11171.
[16] T.-R. Wei, G. Tan, X. Zhang, C.-F. Wu, J.-F. Li, V. P. Dravid, G. J. Snyder, M. G. Kanatzidis, *J. Am. Chem. Soc.* **2016**, *138*, 8875.
[17] L.-D. Zhao, C. Chang, G. Tan, M. G. Kanatzidis, *Energy Environ. Sci.* **2016**, *9*, 3044.
[18] Y. K. Lee, Z. Luo, S. P. Cho, M. G. Kanatzidis, I. Chung, *Joule* **2019**, *3*, 719.
[19] C. Zhou, Y. K. Lee, Y. Yu, S. Byun, Z. Z. Luo, H. Lee, B. Ge, Y. L. Lee, X. Chen, J. Y. Lee, O. Cojocaru-Miredin, H. Chang, J. Im, S. P. Cho, M. Wuttig, V. P. Dravid, M. G. Kanatzidis, I. Chung, *Nat. Mater.* **2021**, *20*, 1378.
[20] Y. Liu, M. Calcabrini, Y. Yu, S. Lee, C. Chang, J. David, T. Ghosh, M. C. Spadaro, C. Xie, O. Cojocaru-Miredin, J. Arbiol, M. Ibanez, *ACS Nano* **2022**, *16*, 78.
[21] Y. Wang, S. Bai, H. Shi, Q. Cao, B. Qin, L.-D. Zhao, *J. Mater. Chem. A* **2023**, *12*, 144.
[22] S. Chandra, U. Bhat, P. Dutta, A. Bhardwaj, R. Datta, K. Biswas, *Adv. Mater.* **2022**, *34*, 2203725.
[23] Y. Qin, B. Qin, T. Hong, X. Zhang, D. Wang, D. Liu, Z.-Y. Wang, L. Su, S. Wang, X. Gao, Z.-H. Ge, L.-D. Zhao, *Science* **2024**, *383*, 1204.
[24] K. Biswas, J. He, I. D. Blum, C. I. Wu, T. P. Hogan, D. N. Seidman, V. P. Dravid, M. G. Kanatzidis, *Nature* **2012**, *489*, 414.
[25] M. Hong, M. Li, Y. Wang, X.-L. Shi, Z.-G. Chen, *Adv. Mater.* **2023**, *35*, 2208272.
[26] Y. Yu, M. Cagnoni, O. Cojocaru-Mirédin, M. Wuttig, *Adv. Funct. Mater.* **2020**, *30*, 1904862.
[27] R. Arora, U. V. Waghmare, C. N. R. Rao, *Adv. Mater.* **2022**, *35*, 2208724.
[28] Y. Sun, L. Zhao, C. J. Pickard, R. J. Hemley, Y. Zheng, M. Miao, *Proc. Natl. Acad. Sci. USA* **2023**, *120*, 2218405120.
[29] L. Hu, B. Duan, T. Lyu, N. Lin, C. Zhang, F. Liu, J. Li, M. Wuttig, Y. Yu, *Adv. Funct. Mater.* **2023**, *33*, 2214854.
[30] Y. Yu, C. Zhou, T. Ghosh, C. F. Schon, Y. Zhou, S. Wahl, M. Raghuwanshi, P. Kerres, C. Bellin, A. Shukla, O. Cojocaru-Miredin, M. Wuttig, *Adv. Mater.* **2023**, *35*, 2300893.
[31] W. Yao, Y. Zhang, T. Lyu, W. Huang, N. Huang, X. Li, C. Zhang, F. Liu, M. Wuttig, Y. Yu, M. Hong, L. Hu, *Innovation* **2023**, *4*, 100522.
[32] D. Sarkar, S. Roychowdhury, R. Arora, T. Ghosh, A. Vasdev, B. Joseph, G. Sheet, U. V. Waghmare, K. Biswas, *Angew Chem Int Ed Engl* **2021**, *60*, 10350.
[33] M. Yan, X. Tan, Z. Huang, G. Liu, P. Jiang, X. Bao, *J. Mater. Chem. A* **2018**, *6*, 8215.
[34] Z. Huang, S. A. Miller, B. Ge, M. Yan, S. Anand, T. Wu, P. Nan, Y. Zhu, W. Zhuang, G. J. Snyder, P. Jiang, X. Bao, *Angew. Chem., Int. Ed. Engl.* **2017**, *56*, 14113.
[35] Y. Wang, B. Qin, T. Hong, L. Su, X. Gao, D. Wang, L.-D. Zhao, *Acta Mater.* **2022**, *227*, 117681.
[36] Y. Luo, S. Hao, S. Cai, T. J. Slade, Z. Z. Luo, V. P. Dravid, C. Wolverton, Q. Yan, M. G. Kanatzidis, *J. Am. Chem. Soc.* **2020**, *142*, 15187.
[37] S. Chandra, R. Arora, U. V. Waghmare, K. Biswas, *Chem. Sci.* **2021**, *12*, 13074.
[38] S. Roychowdhury, T. Ghosh, R. Arora, U. V. Waghmare, K. Biswas, *Angew. Chem., Int. Ed. Engl.* **2018**, *57*, 15167.
[39] M. Dutta, K. Pal, M. Etter, U. V. Waghmare, K. Biswas, *J. Am. Chem. Soc.* **2021**, *143*, 16839.
[40] T. Sriv, T. M. H. Nguyen, Y. Lee, S. Y. Lim, V. Q. Nguyen, K. Kim, S. Cho, H. Cheong, *Sci. Rep.* **2020**, *10*, 11761.
[41] H. J. Zeiger, J. Vidal, T. K. Cheng, E. P. Ippen, G. Dresselhaus, M. S. Dresselhaus, *Phys. Rev. B* **1992**, *45*, 768.
[42] G. C. Cho, W. Kütt, H. Kurz, *Phys. Rev. Lett.* **1990**, *65*, 764.
[43] J.-Y. Raty, M. Wuttig, *J. Phys. D: Appl. Phys.* **2020**, *53*, 234002.
[44] L. Guarneri, S. Jakobs, A. von Hoegen, S. Maier, M. Xu, M. Zhu, S. Wahl, C. Teichrib, Y. Zhou, O. Cojocaru-Miredin, M. Raghuwanshi, C. F. Schon, M. Drogeler, C. Stampfer, R. Lobo, A. Piarristeguy, A. Pradel, J. Y. Raty, M. Wuttig, *Adv. Mater.* **2021**, *33*, 2102356.
[45] B. Gault, A. Chiaramonti, O. Cojocaru-Mirédin, P. Stender, R. Dubosq, C. Freysoldt, S. K. Makineni, T. Li, M. Moody, J. M. Cairney, *Nat. Rev. Methods Primers* **2021**, *1*, 51.
[46] Y. Yu, C. Zhou, S. Zhang, M. Zhu, M. Wuttig, C. Scheu, D. Raabe, G. J. Snyder, B. Gault, O. Cojocaru-Mirédin, *Mater. Today* **2020**, *32*, 260.
[47] Y. Yu, O. Cojocaru-Mirédin, M. Wuttig, *Phys. Status Solidi A* **2023**, 2300425.
[48] F. De Geuser, B. Gault, A. Bostel, F. Vurpillot, *Surf. Sci.* **2007**, *601*, 536.
[49] M. Zhu, O. Cojocaru-Miredin, A. M. Mio, J. Keutgen, M. Kupers, Y. Yu, J. Y. Cho, R. Dronskowski, M. Wuttig, *Adv. Mater.* **2018**, *30*, 1706735.
[50] M. Wuttig, V. L. Deringer, X. Gonze, C. Bichara, J. Y. Raty, *Adv. Mater.* **2018**, *30*, 1803777.
[51] B. J. Kooi, M. Wuttig, *Adv. Mater.* **2020**, *32*, 1908302.
[52] M. Wuttig, C.-F. Schön, J. Lötfering, P. Golub, C. Gatti, J.-Y. Raty, *Adv. Mater.* **2022**, *35*, 2208485.
[53] Y. Cheng, O. Cojocaru-Miredin, J. Keutgen, Y. Yu, M. Kupers, M. Schumacher, P. Golub, J. Y. Raty, R. Dronskowski, M. Wuttig, *Adv. Mater.* **2019**, *31*, 1904316.
[54] C.-F. Schön, S. van Bergerem, C. Mattes, A. Yadav, M. Grohe, L. Kobbelt, M. Wuttig, *Sci. Adv.* **2022**, *8*, eade0828.
[55] J. Y. Raty, M. Schumacher, P. Golub, V. L. Deringer, C. Gatti, M. Wuttig, *Adv. Mater.* **2019**, *31*, 1806280.
[56] G. N. Lewis, *J. Am. Chem. Soc.* **1916**, *38*, 762.
[57] M. Wuttig, D. Lusebrink, D. Wamwangi, W. Welnic, M. Gillessen, R. Dronskowski, *Nat. Mater.* **2007**, *6*, 122.
[58] G. J. Snyder, E. S. Toberer, *Nat. Mater.* **2008**, *7*, 105.
[59] Z. Huang, X. Dai, Y. Yu, C. Zhou, F. Zu, *Scr. Mater.* **2016**, *118*, 19.
[60] M. Hong, W. Lyu, Y. Wang, J. Zou, Z. G. Chen, *J. Am. Chem. Soc.* **2020**, *142*, 2672.
[61] C. Hu, Z. Gao, M. Zhang, S. Han, C. Fu, T. Zhu, *Energy Environ. Sci.* **2023**, *16*, 5381.
[62] X. Zhang, Z. Bu, X. Shi, Z. Chen, S. Lin, B. Shan, M. Wood, A. H. Snyder, L. Chen, G. J. Snyder, Y. Pei, *Sci. Adv.* **2020**, *6*, eabc0726.
[63] Y. Yu, D.-S. He, S. Zhang, O. Cojocaru-Mirédin, T. Schwarz, A. Stoffers, X.-Y. Wang, S. Zheng, B. Zhu, C. Scheu, D. Wu, J.-Q. He, M. Wuttig, Z.-Y. Huang, F.-Q. Zu, *Nano Energy* **2017**, *37*, 203.

[64] Q. Lu, M. Wu, D. Wu, C. Chang, Y. P. Guo, C. S. Zhou, W. Li, X. M. Ma, G. Wang, L. D. Zhao, L. Huang, C. Liu, J. He, *Phys. Rev. Lett.* **2017**, *119*, 116401.
[65] T. Zhu, Y. Liu, C. Fu, J. P. Heremans, G. J. Snyder, X. Zhao, *Adv. Mater.* **2017**, *29*, 1605884.
[66] Z. Liu, T. Hong, L. Xu, S. Wang, X. Gao, C. Chang, X. Ding, Y. Xiao, L. D. Zhao, *Interdisc. Mater.* **2022**, *2*, 161.
[67] G. J. Snyder, A. H. Snyder, M. Wood, R. Gurunathan, B. H. Snyder, C. Niu, *Adv. Mater.* **2020**, *32*, 2001537.
[68] T. Luo, J. J. Kuo, K. J. Griffith, K. Imasato, O. Cojocaru-Mirédin, M. Wuttig, B. Gault, Y. Yu, G. J. Snyder, *Adv. Funct. Mater.* **2021**, *31*, 2100258.
[69] R. Wu, Y. Yu, S. Jia, C. Zhou, O. Cojocaru-Miredin, M. Wuttig, *Nat. Commun.* **2023**, *14*, 719.
[70] K. Peng, H. Wu, Y. Yan, L. Guo, G. Wang, X. Lu, X. Zhou, *J. Mater. Chem. A* **2017**, *5*, 14053.
[71] Y. Yu, M. Wuttig, *Nano Res. Energy* **2023**, *2*, 9120057.
[72] Y. Liu, M. Calcabrini, Y. Yu, A. Genc, C. Chang, T. Costanzo, T. Kleinhanns, S. Lee, J. Llorca, O. Cojocaru-Miredin, M. Ibanez, *Adv. Mater.* **2021**, *33*, 2106858.
[73] N. V. Morozova, I. V. Korobeynikov, N. Miyajima, S. V. Ovsyannikov, *Adv. Sci.* **2022**, *9*, 2103720.
[74] W. Liu, H. S. Kim, Q. Jie, Z. Ren, *Scr. Mater.* **2016**, *111*, 3.
[75] M. K. Brod, M. Y. Toriyama, G. J. Snyder, *Chem. Mater.* **2020**, *32*, 9771.
[76] H. Goldsmid, J. Sharp, *J. Electron. Mater.* **1999**, *28*, 869.
[77] D. Wang, W. He, C. Chang, G. Wang, J. Wang, L.-D. Zhao, *J. Mater. Chem. C* **2018**, *6*, 12016.
[78] S. Bai, X. Zhang, L. D. Zhao, *Acc. Chem. Res.* **2023**, *56*, 3065.
[79] Z.-Y. Huang, F. Wang, C. Jung, S. Zhang, F. Zu, C. Zhou, Y. Yu, *Mater. Today Phys.* **2023**, *37*, 101198.
[80] X. Tang, Z. Li, W. Liu, Q. Zhang, C. Uher, *Interdisc. Mater.* **2022**, *1*, 88.
[81] S. Lee, K. Esfarjani, T. Luo, J. Zhou, Z. Tian, G. Chen, *Nat. Commun.* **2014**, *5*, 3525.
[82] R. Gurunathan, R. Hanus, M. Dylla, A. Katre, G. J. Snyder, *Phys. Rev. Appl.* **2020**, *13*, 034011.
[83] M. Dargusch, X. L. Shi, X. Q. Tran, T. Feng, F. Somidin, X. Tan, W. Liu, K. Jack, J. Venezuela, H. Maeno, T. Toriyama, S. Matsumura, S. T. Pantelides, Z. G. Chen, *J. Phys. Chem. Lett.* **2019**, *10*, 6512.
[84] R. Arora, U. Waghmare, C. N. R. Rao, *Angew. Chem., Int. Ed.* **2024**, *63*, 202313852.
[85] M. Xu, S. Jakobs, R. Mazzarello, J.-Y. Cho, Z. Yang, H. Hollermann, D. Shang, X. Miao, Z. Yu, L. Wang, M. Wuttig, *J. Phys. Chem. C* **2017**, *121*, 25447.
[86] H.-X. Wang, L.-S. Mao, X. Tan, G.-Q. Liu, J. Xu, H. Shao, H. Hu, J. Jiang, *Nano Energy* **2018**, *51*, 649.
[87] K. Thompson, D. Lawrence, D. J. Larson, J. D. Olson, T. F. Kelly, B. Gorman, *Ultramicroscopy* **2007**, *107*, 131.
[88] J. Keutgen, A. J. London, O. Cojocaru-Miredin, *Microsc. Microanal.* **2020**, *27*, 28.
[89] P. E. Blöchl, *Phys. Rev. B* **1994**, *50*, 17953.
[90] M. Kohout, *DGrid, version 4.7*, Radebeul, Germany **2019**.
[91] A. Otero-de-la-Roza, E. R. Johnson, V. Luaña, *Comput. Phys. Commun.* **2014**, *185*, 1007.
[92] R. F. W. Bader, M. E. Stephens, *J. Am. Chem. Soc.* **1975**, *97*, 7391.
[93] G. Kresse, J. Furthmüller, *Phys. Rev. B* **1996**, *54*, 11169.
[94] J. P. Perdew, K. Burke, M. Ernzerhof, *Phys. Rev. Lett.* **1996**, *77*, 3865.
[95] J. P. Perdew, K. Burke, Y. Wang, *Phys. Rev. B* **1996**, *54*, 16533.
[96] W. Setyawan, S. Curtarolo, *Comput. Mater. Sci.* **2010**, *49*, 299.
[97] V. Wang, N. Xu, J.-C. Liu, G. Tang, W.-T. Geng, *Comput. Phys. Commun.* **2021**, *267*, 108033.
[98] A. Kokalj, *J Mol Graph Model* **1999**, *17*, 176.
[99] S. Lany, A. Zunger, *Phys. Rev. B* **2008**, *78*, 235104.
[100] C. G. Van de Walle, J. Neugebauer, *J. Appl. Phys.* **2004**, *95*, 3851.